

## Effect of fluids and frequencies on Poisson's ratio of sandstone samples

Lucas Pimienta<sup>1</sup>, Jérôme Fortin<sup>1</sup>, and Yves Guéguen<sup>1</sup>

### ABSTRACT

Poisson's ratio  $\nu$  is an important parameter when interpreting measured geophysical and seismic data. For an isotropic medium, it directly relates to the ratio of P- and S-wave velocities. We have measured  $\nu$  as a function of pressure and frequency in fluid-saturated sandstones. The method of measuring  $\nu$  was first tested as a function of pressure and frequency using standard samples. The phase shift  $\varphi$  between radial and axial strains was also measured. For all standard samples, such as the linear viscoelastic Plexiglas, the data indicated that  $\tan(\varphi)$  correlated with  $\nu$  and related to a dissipation on  $\nu$ . Then,  $\nu$  and  $\tan(\varphi)$  were measured as a function of pressure and frequency for two dry and fluid-saturated Fontainebleau sandstone samples. Under dry conditions, no frequency dependence and very small pressure dependence were observed. Unusual behaviors were observed under fluid-saturated conditions. In particular,  $\nu$  of one sample indicated a frequency-

dependent bell-shaped dispersion under water and glycerin saturation that correlated with peaks in  $\tan(\varphi)$ . Plotting the measurements as a function of apparent frequency (i.e., normalizing by the fluid viscosity) indicated a good fit between the water- and glycerin-saturated measurements. The bell-shaped dispersion in  $\nu$  that was observed for one particular sandstone held for all effective pressures. These variations fully correlated with the peaks of  $\tan(\varphi)$  observed. Our results can be interpreted using fluid flow and effective medium theories in the case of a porous microcracked rock. Drained/undrained and relaxed/unrelaxed transitions have frequency and magnitude of variations that are consistent with the measurements. The rock sample microcrack density strongly affects this frequency dependence. The inferred  $V_P/V_S$  ratio at low effective pressures also indicates a large frequency-dependent bell-shaped dispersion. The parameter  $\tan(\varphi)$  is a clear indicator of the frequency-dependent dissipation of  $\nu$  and relates to the attenuation of P- and S-waves.

### INTRODUCTION

Sedimentary rocks saturated by fluids are known to be dispersive materials. Their frequency-dependent behaviors originate from fluid movements in the rocks' porous network (e.g., Müller et al., 2010). When comparing field and laboratory measurements, the frequency dependence of the elastic properties is to be considered. The usual properties sought are P- and S-wave velocities. Their ratio is known to relate to Poisson's ratio, an intrinsic property of a given material.

Stress-strain experiments are promising methods to characterize the dispersive properties of rocks. Elastic measurements are performed over wide frequency  $f$  and confining pressure  $P_c$  ranges of  $f \in [10^{-3}; 10^3]$  Hz and  $P_c \in [0; 100]$  MPa, respectively (e.g., Subramanyan et al., 2014). Apparatuses for measurements of hydrostatic (Adelinet et al., 2010; David et al., 2013; Fortin et al., 2014;

Pimienta et al., 2015a) or shear (Jackson and Paterson, 1987) stress oscillations have been developed, but the stress-strain method applied to axial stress oscillations is by far the most widely used (e.g., Batzle et al., 2001, 2006; Adam et al., 2006, 2009; Mikhal'tsevitch et al., 2011; Tisato and Madonna, 2012; Madonna and Tisato, 2013; Pimienta et al., 2015b). To the authors' knowledge, data found in the literature mostly report and investigate the frequency dependence of the measured Young's modulus and attenuation, or of inferred moduli or velocities (e.g., Adam et al., 2006, 2009; Batzle et al., 2006). The rock Poisson's ratio can also be measured from such a setup. Yet, the frequency dependence of this elastic coefficient is not often specifically investigated. To the authors' knowledge, only Mikhal'tsevitch et al. (2013) report Poisson's ratio measured as a function of frequency, and Adam and Batzle (2008) report the inferred  $V_P/V_S$  for different frequencies. In their case, Poisson's ratio was found to be frequency independent.

Manuscript received by the Editor 11 June 2015; revised manuscript received 3 November 2015; published online 09 March 2016.

<sup>1</sup>PSL Research University, Laboratoire de Géologie de l'ENS, Paris, France. E-mail: pimienta@geologie.ens.fr; fortin@geologie.ens.fr; gueguen@geologie.ens.fr.

© 2016 Society of Exploration Geophysicists. All rights reserved.

Using three standard samples, Poisson's ratio  $\nu$  and the phase shift  $\tan(\phi)$  between the radial and axial strain are measured in the frequency and pressure ranges of  $f \in [5.10^{-3}; 10^2] \text{ Hz}$  and  $P_c \in [0; 30] \text{ MPa}$ . Several measurements are subsequently obtained in fluid-saturated sandstone samples. Fluid-flow, poroelastic, and effective medium theories are used to interpret the experimental results.

## SAMPLES AND METHOD

### Samples

#### Calibration samples

The experimental setup and procedure were tested using three standard samples: (1) a synthetic glass sample (Mallet et al., 2013), (2) a pure gypsum sample (Brantut et al., 2012), and (3) a Plexiglas (poly[methyl methacrylate] PMMA) sample (e.g., Batzle et al., 2006). These samples (1) are homogeneous and isotropic media at the sample scale, (2) show a large range in elastic moduli values, and (3) have no porosity, and their elastic properties are independent of the applied stresses. Glass and gypsum elastic properties are independent of frequency, but Plexiglas is a linear viscoelastic material whose moduli are frequency dependent. Although known to show properties that slightly vary depending on the manufacturing condition, Plexiglas is often used to test an attenuation apparatus (e.g., Batzle et al., 2006; Tisato and Madonna, 2012; Madonna and Tisato, 2013; Pimienta et al., 2015a, 2015b).

#### Fontainebleau sandstone

Fontainebleau sandstone is a well-known reference rock. Framework grains and cement are pure quartz, making up a clean sandstone of approximately 99.9% quartz (Bourbie and Zinszner, 1985; Gomez et al., 2010). The rock possesses a random grain orientation and is well sorted, with an average grain size of approximately 200  $\mu\text{m}$ . It can consistently be assumed to be homogeneous and isotropic at the representative elementary volume scale (i.e., volume  $\gg$  grains volume).

Depending on the amount of cementing quartz, the porosity  $\phi$  of Fontainebleau sandstone samples ranges from 2% for highly cemented samples to 25% for poorly cemented samples. The main differences between samples are the pores' entry diameters. These diameters decrease from  $d \sim 20 \mu\text{m}$  (high porosity) to  $d \sim 5 \mu\text{m}$  (low porosity), which leads to variations in permeability ranging over four to five orders of magnitude (Bourbie and Zinszner, 1985). Furthermore, independently of the porosity and degree of cement, Fontainebleau sandstone is a rock with a wide range in microcrack density (e.g., Pimienta et al., 2014).

We measure two samples with a porosity of  $\phi = 7.3\%$  (Fo7) and  $\phi = 8.3\%$  (Fo8). The same samples have been investigated previously for dispersion/attenuation data of the rocks' Young's modulus (Pimienta et al., 2015b). In addition, samples from the same blocks have been used to investigate the dispersion/attenuation of the rocks' bulk modulus (Pimienta et al., 2015a).

### Processing method

An apparatus able to apply sinusoidal stress of small amplitude is used for the study. The sample's axial and radial strains are directly measured on the sample from strain gauges glued at the sample's

half-length. The fluid pressure is maintained constant at  $P_p = 3 \text{ MPa}$ . Terzaghi effective pressure is defined as  $P_{\text{eff}} = P_c - P_p$ . The experimental apparatus and procedure have been detailed in Pimienta et al. (2015b). From the directly measured axial and radial strains, we get the strain amplitude and phase. We assume that, at the low strain amplitudes of our experiment, linear viscoelasticity holds. Therefore, in the frequency domain, moduli are complex valued with real and imaginary parts, for example,  $\nu^* = \nu_1 + i\nu_2$  for Poisson's ratio. The real part is obtained from the amplitude of the strain signals. The phase shift between radial and axial strains is directly related to the imaginary part. Here, we investigate the measurements on Poisson's ratio  $\nu = \nu_1$  and its associated dissipation  $\tan(\phi) = \nu_2/\nu_1$ .

#### Strains amplitude: Poisson's ratio $\nu$

The confining pressure is maintained constant (i.e.,  $\Delta P_c = 0$ ), and an oscillating axial stress is exerted on the sample (i.e.,  $\Delta\sigma_{\text{ax}} \neq 0$ ). For each  $\Delta\sigma_{\text{ax}}$  frequency, axial and radial strains are recorded and the low-frequency Young's modulus  $E$  and Poisson's ratio  $\nu$  are inferred (e.g., Batzle et al., 2006). A typical processing method is applied to the signal (Pimienta et al., 2015a), namely, phase picking in the frequency domain after the Fourier transform (e.g., Batzle et al., 2006; Madonna and Tisato, 2013; Mikhaltsevitch et al., 2014) to obtain the phase shifts and filtering in the frequency domain.

The sample Poisson's ratio  $\nu$  is obtained from a linear regression between radial and axial strains. The data scatter around the linear regressions is used to infer a statistical error, noted as  $\Delta\nu$ . Owing to the recording limitations, strains with peak-to-peak amplitudes lower than approximately  $5-8 \times 10^{-7}$  cannot be precisely measured. Because the quartz Poisson's ratio  $\nu_{\text{qtz}}$  is slightly less than 0.1 (e.g., Mavko et al., 2003) and the radial strains cannot be measured for strains lower than  $\Delta\epsilon \sim 5-8 \times 10^{-7}$ , axial strains are fixed to be lower than  $5-8 \times 10^{-6}$ . As shown by previous authors (e.g., Winkler and Murphy, 1995), a dependence to the strain amplitude could be observed in rocks for strain "maximum" amplitudes more than  $10^{-6}$ . However, note that these authors refer to very porous and loosely cemented sandstones. For example, the Massilon sandstone has a porosity of approximately  $\phi = 24.6\%$  (Winkler, 1983). Fo7 and Fo8 samples are much less porous and much more cemented sandstones. Moreover, Winkler and Murphy (1995) measure a decrease of only 1.2% in Young's modulus for a "maximum" strain of  $5 \times 10^{-6}$  (i.e., a peak-to-peak strain amplitude of  $10^{-5}$ ) in Massilon sandstone. This effect is small. Therefore, we can conclude that, in our experiment, deformations are in the linear elastic domain, for strain peak-to-peak amplitudes lower than approximately  $10^{-5}$ .

#### Strains phase: Radial to Axial phase shift $\tan(\phi)$

Assuming an isotropic linear viscoelastic medium in which the moduli imaginary parts remain small (Winkler and Nur, 1979), Young's modulus and bulk modulus inverse quality factors and  $Q_K^{-1}$  can be defined. From typical stress-strain experiments,  $Q_E^{-1}$  and  $Q_K^{-1}$  are defined as the tangent of the phase shift between stress and strain, that is, the phase shift between the two end-members used to calculate  $E$  and  $K$ . Similarly, one may investigate the tangent of the phase shift between the two end-members used to calculate  $\nu$ , that is, the phase shift  $\phi$  between radial and axial strains.

At this stage, it is of interest to examine the physical meaning of the measured  $\tan(\varphi)$ . The attenuation coefficient  $\gamma$  is a coefficient that is uniquely defined in the case of waves traveling through a medium. The amplitude of the wave varies as  $e^{-\gamma x}$  after propagation over a distance  $x$ . The inverse quality factor  $Q^{-1}$  is directly related to  $\gamma$ . Quality factors are defined for the elastic moduli  $K$ ,  $G$ , and  $E$  (Winkler and Nur, 1979; Mavko et al., 2003; Adam et al., 2009). By analogy with the elastic moduli, one could define Poisson's ratio associated quality factor  $Q_\nu^{-1} = \tan(\varphi)$ .

Relations between  $Q_K^{-1}$ ,  $Q_E^{-1}$ , and  $Q_P^{-1}$  and  $Q_S^{-1}$  (i.e., the P- and S-wave attenuations) are known (Winkler and Nur, 1979) by assuming that the complex moduli can be substituted for their corresponding real moduli in the linear elasticity relations and the attenuation (i.e.,  $Q^{-1}$ ) is equal to the ratio between the imaginary  $\text{Im}(M)$  and real  $\text{Re}(M)$  part of the modulus  $M$ . The shear modulus quality factor  $Q_G$  is equal to the shear-wave attenuation  $Q_S$ . In isotropic and slightly dissipative media, Winkler and Nur (1979) indeed show that  $Q_K$  or  $Q_E$  can be explicitly defined as a function of  $Q_P$  and  $Q_S$  such that:

$$\frac{(1-x)(1-2x)}{Q_P} = \frac{(1+x)}{Q_E} - \frac{2x(2-x)}{Q_S}, \quad (1)$$

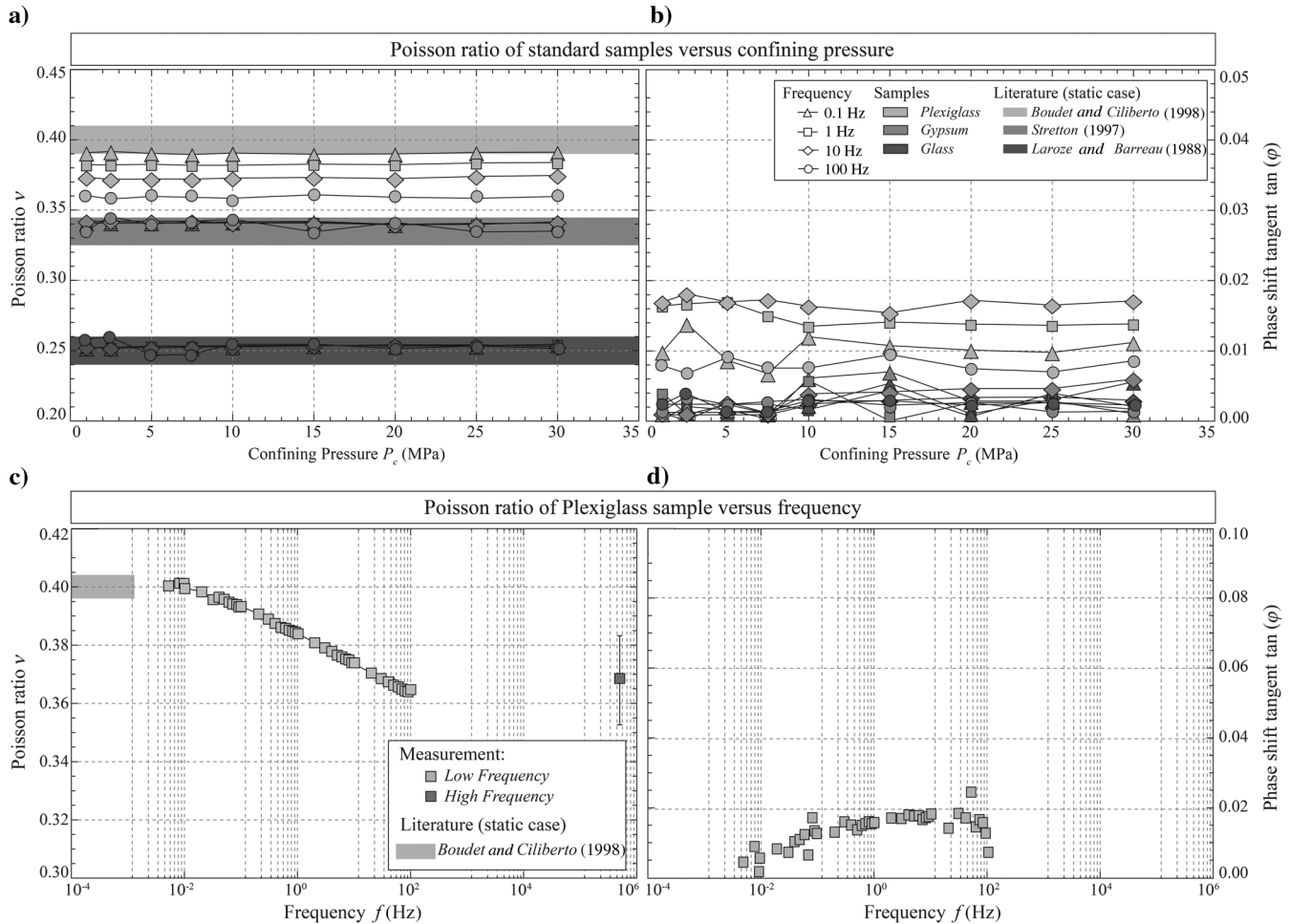


Figure 1. Measured (a) Poisson's ratio  $\nu$  and (b) phase shift  $\tan(\varphi)$  as a function of pressure for the three standard samples at four frequencies of  $f = [0.1; 1; 10; 100]$  Hz. Data from the literature, measured under static conditions (Bouget and Ciliberto, 1998), are reported for comparison. The frequency-dependent (c)  $\nu$  and (d)  $\tan(\varphi)$  is also reported for the Plexiglas sample for a confining pressure of  $P_c = 10$  MPa.

$$\frac{(1-2x)}{Q_K} = \frac{3}{Q_E} - \frac{2(1+x)}{Q_S}, \quad (2)$$

$$\frac{(1+x)}{Q_K} = \frac{3(1-x)}{Q_P} - \frac{2(1-2x)}{Q_S}, \quad (3)$$

where  $x$  has been previously assumed (e.g., Winkler and Nur, 1979) to be the rock Poisson's ratio  $\nu$ . Indeed, in the previous works,  $\nu$  has been considered to be real valued. This assumption is not consistent. The reason is simple: If  $K$  and  $G$  (or  $E$ ) are complex valued, it follows that the same is true for  $\nu$ . Defining a complex-valued Poisson's ratio  $\nu^* = \nu_1 + i\nu_2$ , using the relationship of linear isotropic viscoelasticity between  $\nu^*$ ,  $E^*$ , and  $G^*$ , that is  $E^* = G^*(1 + \nu^*)$ , one gets the following:

$$\nu^* = \nu_1 + i\nu_2 = \frac{(E_1 + iE_2) - 2(G_1 + iG_2)}{2(G_1 + iG_2)}, \quad (4)$$

where  $E_1$  and  $G_1$  are the real parts, and  $E_2$  and  $G_2$  are the imaginary parts associated with  $E^*$  and  $G^*$ . Note that here, the real part of  $\nu^*$  is  $\nu_1 = (G_1(E_1 - 2G_1) + G_2(E_2 - 2G_2))/2(G_1^2 + G_2^2)$ , and not  $x = (E_1/2G_1) - 1$ . Assuming the medium to be slightly dissipa-

pative,  $E_2$  and  $G_2$  are smaller than  $E_1$  and  $G_1$  so that  $(E_2 G_2) \ll (E_1 G_1)$  and  $G_2^2 \ll G_1^2$ . Thus, the relation of linear elasticity would be obtained such that  $\nu_1 \sim x = (E_1/2G_1) - 1$ .

Further multiplying by the conjugate part, extracting real and imaginary parts, and defining the associated quality factor  $Q_\nu^{-1} = (\nu_2/\nu_1)$ , one obtains the following relationship:

$$Q_\nu^{-1} = \frac{\nu_2}{\nu_1} = \frac{E_2 G_1 - E_1 G_2}{G_1(E_1 - 2G_1) + G_2(E_2 - 2G_2)}. \quad (5)$$

Noting that  $Q_E^{-1} = (E_2/E_1)$  and  $Q_S^{-1} = Q_G^{-1} = (G_2/G_1)$ , one finally obtains the relationship between  $Q_\nu^{-1}$ ,  $Q_E^{-1}$ , and  $Q_S^{-1}$  such that:

$$Q_\nu^{-1} \left[ x + \frac{1}{Q_S} \left( \frac{1+x}{Q_E} - \frac{1}{Q_S} \right) \right] = \frac{1+x}{Q_E} - \frac{1+x}{Q_S}, \quad (6)$$

where  $x = (E_1/2G_1) - 1$  is the same unknown parameter as in equations 1, 2, and 3, which would correspond to Poisson's ratio if this property was nondispersive. From equation 1,  $Q_E^{-1}$  can be defined as a function of  $Q_P^{-1}$  and  $Q_S^{-1}$ . Thus,  $Q_\nu^{-1}$  can also be directly defined as a function of  $Q_P^{-1}$  and  $Q_S^{-1}$ , that is, the P- and S-wave attenuations. As a consequence, the measured frequency-dependent variations in  $\tan(\phi) = Q_\nu^{-1}$  are expected to relate to an attenuation on the P- and S-waves.

## RESULTS

### Poisson's ratio of standard samples

For the three standard samples, the pressure dependence of  $\nu$  and  $\tan(\phi)$  is investigated (Figure 1a and 1b) for the measured frequencies of  $f = [0.1; 1; 10; 100]$  Hz. Consistently, the measured  $\nu$  (Figure 1a) in glass and gypsum samples fits with the literature data and  $\tan(\phi)$  (Figure 1b) remains lower than 0.01 for all frequencies and pressures for both samples. Only for the viscoelastic Plexiglas sample, a deviation from the static measurement is observed on  $\nu$ . For this viscoelastic sample,  $\nu$  and  $\tan(\phi)$  vary with frequency at all pressures.

For the Plexiglass sample,  $\nu$  and  $\tan(\phi)$  are reported (Figure 1c and 1d) in the frequency range of  $f \in [10^{-3}; 10^2]$  Hz. The measured  $\nu$  (Figure 1c) shows a variation that is consistent with the static value  $\nu = 0.4$  reported (Boudet and Ciliberto, 1998) and the value  $\nu_{HF} \sim 0.36$  inferred from ultrasonic velocities (Pimienta et al., 2015a). The decrease appears to be continuous in the frequency range of the study. Consistently, this variation correlates with a broad peak of  $\tan(\phi)$  (Figure 1d). The Plexiglas sample is a known linear viscoelastic material that exhibits elastic dispersion/attenuation behavior of its bulk modulus (Pimienta et al., 2015a) and Young's modulus (Batzle et al., 2006; Madonna et al., 2011; Tisato and Madonna, 2012; Pimienta et al., 2015b). From the Kramers-Kronig relations, it is known that, for a linear viscoelastic material, dispersion and attenuation are related. Our data on Plexiglas show that the experimental apparatus is reliable and can provide accurate estimates of dispersion and attenuation.

### Dependence on fluids and frequencies at $P_{eff} = 1$ MPa

Poisson's ratio  $\nu$  and phase shift  $\tan(\phi)$  of both fluid-saturated Fontainebleau samples are reported as a function of frequency at the lowest effective pressure of  $P_{eff} = 1$  MPa (Figure 2). For  $\nu$

(Figure 2a) and  $\tan(\phi)$  (Figure 2b), a large difference in behavior is observed between the two samples. For sample Fo8, small variations in Poisson's ratio are observed for different fluids and frequencies. Simultaneously, low values (i.e.,  $\tan(\phi) < 0.03$ ) and variations in  $\tan(\phi)$  are measured.

By contrast, Poisson's ratio of sample Fo7 highlights an unusual behavior of frequency-dependent bell-shaped variations under water  $\nu_{wat}$  and glycerin  $\nu_{gly}$  saturation;  $\nu$  increases with frequency up to a characteristic frequency value beyond which it decreases. The peaks of the bell-shaped variations of  $\nu_{wat}$  and  $\nu_{gly}$  have the same magnitudes, but they are shifted in frequency. Under water saturation, two  $\tan(\phi)$  peaks (Figure 2b) of small amplitude (i.e., 0.05) are measured. The first peak, at  $f = 5$  Hz, correlates with the increase in  $\nu_{wat}$ . The second peak, at  $f = 60$  Hz, correlates with the decrease in  $\nu_{wat}$ . Under glycerin saturation, a double peak in  $\tan(\phi)$ , with a maximum amplitude of 0.15, is measured above  $f = 0.1$  Hz. This peak correlates to the continuous decrease in  $\nu_{gly}$ .

### Effect of pressure for Fo7

Sample Fo8 shows a small variation of  $\nu$  with frequency. The behavior of the Fo7 sample is very different. We further investigate the effect of effective confining pressure on Fo7 properties.

#### Pressure dependence for different saturating fluids

The pressure dependence of Poisson's ratio  $\nu$  of Fo7 under dry, water-saturated, and glycerin-saturated conditions is reported (Figure 3) for four measured frequencies of  $f = [0.1; 1; 10; 100]$  Hz.

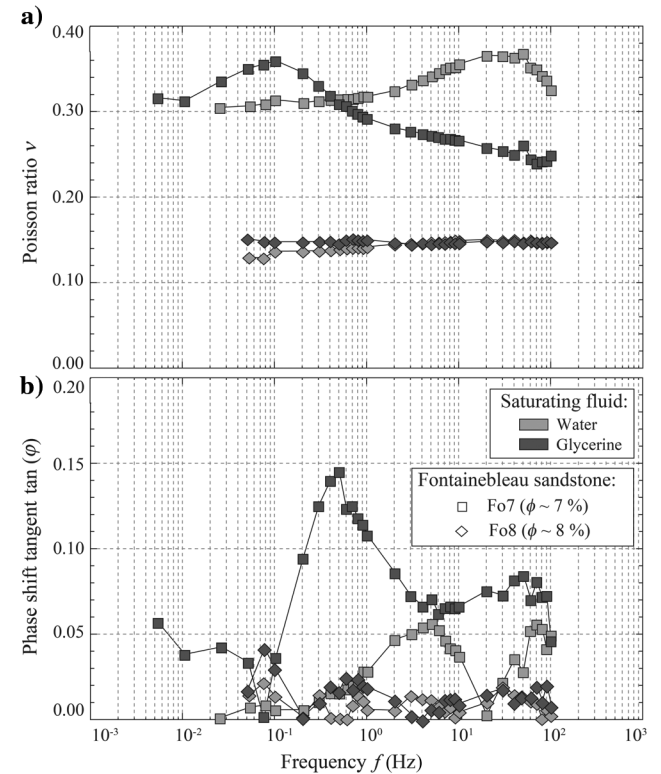


Figure 2. Measured frequency-dependent (a) Poisson's ratio  $\nu$  and (b) phase shift  $\tan(\phi)$  of samples Fo7 and Fo8 saturated by either water or glycerin at a pressure of  $P_{eff} = 1$  MPa.

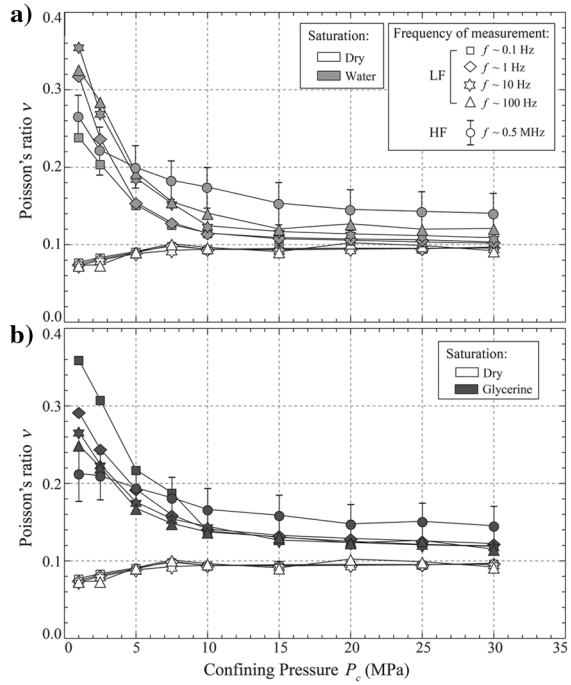


Figure 3. Measured pressure dependent Poisson's ratio of Fo7 saturated by either (a) water or (b) glycerine. The added axial load applied for the measurement's stability was  $\sigma_{ax} = 0.2$  MPa.

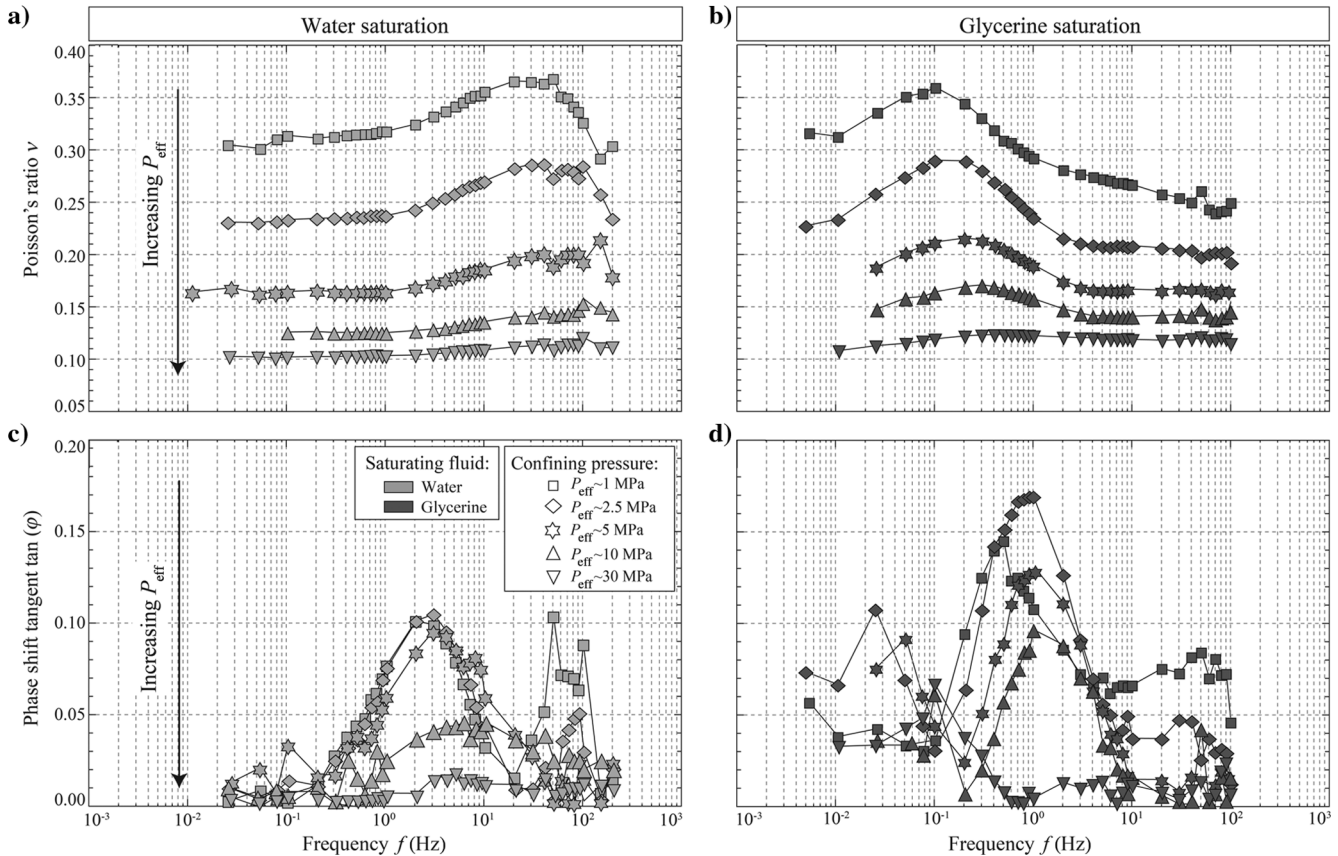


Figure 4. Frequency dependence of the (a) Poisson's ratio  $\nu$  and (b) phase shift tangent  $\tan(\phi)$  of the 7% porosity Fontainebleau sandstone sample (i.e., Fo7) saturated by either water or glycerin. The measurements are obtained at different effective pressures of  $P_{eff} = [1; 2.5; 5; 10; 30]$  MPa.

The measurements under dry conditions are compared with the ones under either water- (Figure 3a) or glycerin-saturated (Figure 3b) conditions.

Under dry conditions, an increase in  $\nu_{dry}$  (Figure 3) is measured with increasing confining pressure. This behavior is expected in isotropic rocks if microcracks are progressively closed by the increasing pressure (Wang et al., 2012). When saturating the rock by a low-compressibility fluid (i.e., water or glycerin),  $\nu$  significantly increases with respect to the dry rock measurements. The effective pressure strongly damps the differences between dry and fluid-saturated  $\nu$ , so that all measurements converge to a  $\nu$  value near 0.1 at  $P_{eff} = 30$  MPa. At low  $P_{eff}$ , however, the frequency dependence differs for the two saturating fluids. Under water saturation, the maximum for  $\nu$  is attained for a frequency of  $f = 10$  Hz. Beyond this frequency, values of  $\nu$  are lower. This behavior is consistent with the frequency-dependent bell-shaped variation observed at  $P_{eff} = 1$  MPa (Figure 2). Under glycerin saturation, in agreement with Figure 2,  $\nu$  reaches its maximum value at  $f = 0.1$  Hz. Beyond that frequency,  $\nu$  decreases.

#### Evolution of the frequency dependence with pressure

The frequency dependence of Poisson's ratio is reported (Figure 4) in the case of the Fo7 sandstone sample saturated by either water or glycerin. The pressures of measurements are  $P_{eff} = [1; 2.5; 5; 10; 30]$  MPa. For both saturating fluids, large frequency-dependent variations of  $\nu$  and  $\tan(\phi)$  are observed.

For any  $P_{\text{eff}}$  below 30 MPa, the frequency-dependent bell-shaped curve of  $\nu$  is observed under water and glycerin saturations. Yet, the amplitude of variations and the maximum values of  $\nu$  decrease when  $P_{\text{eff}}$  increases. Again, for all  $P_{\text{eff}}$ , the maximum values of  $\nu$  are identical for both fluids, but the variations are shifted in frequency. Under water saturation (Figure 4a), the maxima occur at approximately 20–50 Hz. Under glycerin saturation (Figure 4b), the maximum is observed at lower frequencies, of approximately 0.1 Hz. Note that the  $\nu$  maxima shift to slightly higher frequencies as  $P_{\text{eff}}$  increases.

The phase shifts  $\tan(\varphi)$  measured under either water (Figure 4c) or glycerin (Figure 4d) saturation show peaks of similar magnitudes but at different frequencies. For both saturating fluids, two  $\tan(\varphi)$  peaks are observed in the investigated frequency range that correlate with the measured dispersion in  $\nu$ . The first peak, at approximately 3 Hz for water and approximately 0.02 Hz for glycerin, takes place in a frequency range where  $\nu$  increases. The second one, at approximately 70 Hz for water and approximately 1 Hz for glycerin, takes place in a frequency range in which  $\nu$  decreases.

## INTERPRETATION: FLUID FLOW AND EFFECTIVE MEDIUM THEORY

The frequency dependence of elastic properties in fluid-saturated rocks is understood as a result of fluid flow at different scales that induces transitions between distinct elastic regimes (e.g., Müller et al., 2010). We discuss below the interpretations in terms of existing theories. First, the overall frequency dependence is investigated in the light of fluid-flow theories. Then, the effect of the boundary conditions in the experimental setup is discussed using the theory of poroelasticity. Finally, effective medium theories are used to estimate values of Poisson's ratio in the three elastic regimes.

### Fluid-flow theories: Frequency dependence of elastic properties

Three main regimes are expected in the frequency range of our study (e.g., Müller et al., 2010): the drained, undrained, and unrelaxed regimes. In the drained regime, fluid can freely flow in and out of a representative elementary volume (REV) of the sample, so that the fluid compressibility does not affect the sample's overall compressibility. Thus, the elastic properties are the ones of the dry sample. In the undrained regime, fluid is not allowed to flow out of the REV, and its pressure increases. Consequently, the sample's overall compressibility decreases. Drained and undrained regimes are isobaric (i.e., relaxed) at the scale of the REV. That is, all inclusions inside the REV are connected and pore fluid pressure in the REV is constant. The third, unrelaxed, elastic regime is a regime in which the inclusions inside the REV are not isobaric because local fluid flow has not had enough time to take place. The fluid overpressure in the unrelaxed regime will then directly depend on the inclusion's geometry, that is, larger in the more compliant penny-shaped microcracks and lower inside the spherical pores.

In the framework of the fluid flow theories, these three elastic regimes may be related in frequency. Indeed, two transitions between the three elastic regimes are expected (e.g., Sarout, 2012) in the seismological/seismic frequency range ( $f \in [10^{-3}; 10^6]$  Hz). A characteristic frequency can be inferred for each transition. The first transition is from drained to undrained regimes (both are “relaxed,” poroelastic, regimes), and is controlled by the time constant (or

critical frequency  $f_1$ ) for the fluid to flow over the sample's length  $L$  (Cleary, 1978) as follows:

$$f_1 = \frac{4kK_d}{\eta_f L^2}, \quad (7)$$

where  $k$  and  $K_d$  are the rock permeability and the drained bulk modulus, respectively, and  $\eta_f$  is the fluid viscosity. The second transition is from undrained (relaxed) to unrelaxed regimes, and it is ruled by the time constant (or critical frequency  $f_2$ ) for fluid flow out of the rocks' microcracks (O'Connell and Budiansky, 1977; Mavko et al., 2003) as follows:

$$f_2 = \frac{\xi^3 K_d}{\eta_f}, \quad (8)$$

where  $\xi$  is the averaged microcrack aspect ratio.

The  $f_1$  and  $f_2$  are inversely proportional to the fluid's viscosity  $\eta_f$ , so that apparent frequency  $f^*$  that accounts for fluid's viscosity  $\eta_f$  can be defined as follows:

$$f^* = f \frac{\eta_f}{\eta_0}, \quad (9)$$

where  $\eta_0 = 10^{-3}$  Pa · s and  $\eta_f$  is the fluid viscosity. To obtain a direct in situ measurement of fluids' viscosity, the hydraulic conductivity ( $\kappa/\eta$ ) is measured as a function of the effective pressure. Assuming the same permeability values for both fluids (which may not be exactly true), the ratio between fluid in situ viscosities is

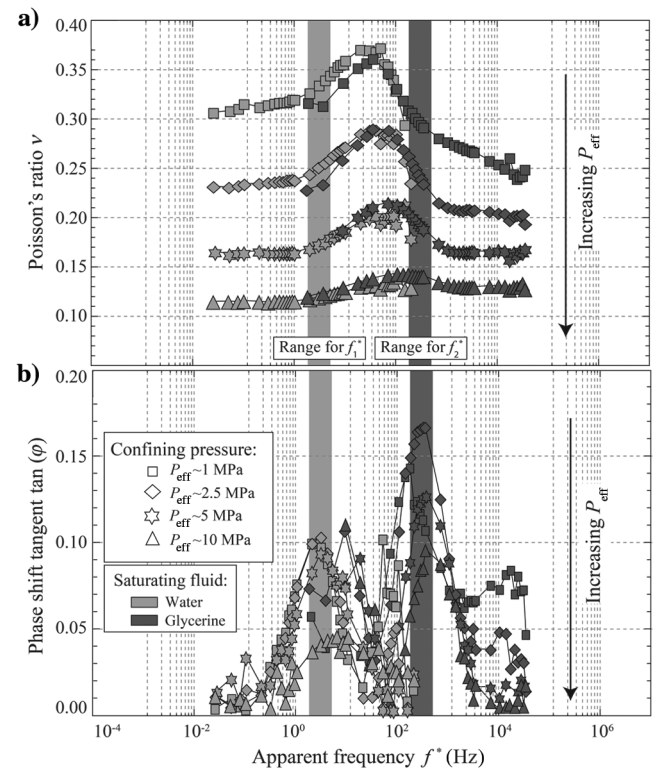


Figure 5. Inferred dependence on apparent frequency  $f^*$  of (a)  $\nu$  and (b)  $\tan(\varphi)$  for the 7% Fontainebleau sandstone (Fo7). Measurements are performed for effective pressures of  $P_{\text{eff}} = [1; 2.5; 5; 10]$  MPa. The cutoff frequencies  $f_1^*$  and  $f_2^*$  are obtained from the  $\tan(\varphi)$  peaks.

found to be  $\eta_{\text{wat}}/\eta_{\text{gly}} \sim 350$  (Pimienta et al., 2015b). Given that the experimental range of  $f$  is  $[510^{-3}; 10^2]$  Hz, the apparent frequency range is (1) of  $f_{\text{wat}}^* \in [510^{-3}; 10^2]$  Hz for water saturation (i.e.,  $\eta_{\text{wat}} = 10^{-3}$  Pa · s) and (2) of  $f_{\text{gly}}^* \in [1.75; 0.3510^5]$  Hz for glycerin saturation (i.e.,  $\eta_{\text{gly}} = 0.35$  Pa · s). The critical frequencies can also be redefined as  $f_1^*$  and  $f_2^*$ . Using values for  $K_d$ ,  $k$ , and  $\xi$  obtained for this rock at  $P_{\text{eff}} = 1$  MPa (Pimienta et al., 2015a),  $f_1^*$  and  $f_2^*$  are at approximately 10 Hz and 1 kHz, respectively, for this rock sample.

Poisson's ratio  $\nu$  and  $\tan(\varphi)$  are plotted against apparent frequency for different pressures of  $P_{\text{eff}} = [1; 2.5; 5; 10]$  MPa (Figure 5). The frequencies allowed by the apparatus lead to measurements under different fluid saturations that have the same apparent frequency. A good fit is obtained between measurements. Interestingly, the maximum values of  $\nu_{\text{gly}}$  and  $\nu_{\text{wat}}$  are identical for all effective pressures (Figure 5a). Bell-shaped curves are observed over the complete  $f^*$  range.

The measured  $\tan(\varphi)$  (Figure 5b) under water and glycerin saturations is also consistent. Two  $\tan(\varphi)$  peaks are observed. The characteristic frequencies of the  $\tan(\varphi)$  peaks are found to be of 5 and 500 Hz, respectively, which are near the predicted values of  $f_1^* = 10$  Hz and  $f_2^* = 1$  kHz. Thus, the measured Poisson's ratio  $\nu$  dispersions and  $\tan(\varphi)$  values seem a very good proxy of both transitions between elastic regimes.

As  $P_{\text{eff}}$  increases, the magnitude in  $\nu$  variations decreases. This is likely due to closure of preexisting microcracks. Furthermore, note

that the characteristic frequency for the maximum of  $\nu$  slightly increases as  $P_{\text{eff}}$  increases, that is, from  $f \sim 30$  Hz at  $P_{\text{eff}} = 1$  MPa up to  $f \sim 100$  Hz at  $P_{\text{eff}} = 10$  MPa. This could be the consequence of a  $K_d$  increase with  $P_{\text{eff}}$ .

## Discussion of the experimental boundary conditions

Note from Figure 5 the large difference, especially at low  $P_{\text{eff}}$ , observed between the dry (e.g., 0.07 at  $P_{\text{eff}} = 1$  MPa) and fluid-saturated drained (e.g., 0.3 at  $P_{\text{eff}} = 1$  MPa) Poisson's ratio. This effect may be explained by the experimental boundary conditions (e.g., Dunn, 1987), not allowing for a total fluid flow out of the sample. Two possible effects can add up: (1) the lateral jacketing of the sample, preventing lateral fluid flow, and (2) the existence of a dead volume at both samples' ends (Pimienta et al., 2015a). Here, we investigate the sole effect of the dead volume.

Owing to the existence of a dead volume, the fluid over-pressure cannot relax completely and attain the value of zero over-pressure that characterizes the purely drained condition. To account for this effect, a first-order correction can be applied by assuming that, locally (i.e., at the place in which strain gauges are glued), the fluid over-pressure is  $p_f$  and not zero. From linear poroelasticity, axial  $\epsilon_{\text{ax}}^*$  and radial  $\epsilon_{\text{rad}}^*$  strains are a function of axial load  $\sigma_{\text{ax}}$  and pore pressure  $p_f$  such that (e.g., Detournay and Cheng, 1993)

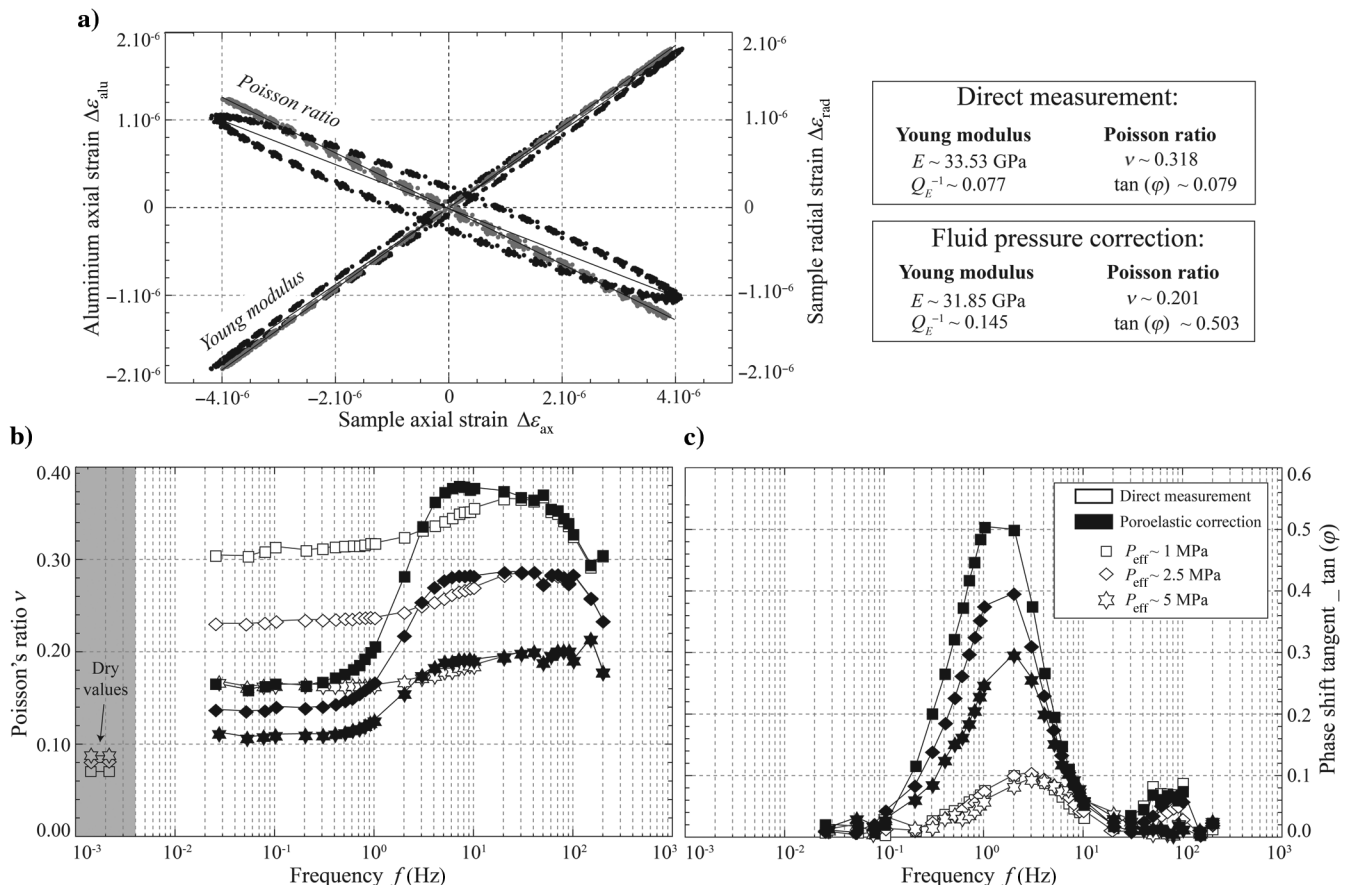


Figure 6. (a) Example of the fluid pressure correction on  $E$  and  $\nu$  for sample Fo7 measured under water saturation. Example of the frequency-dependent variations of the corrected (b)  $\nu$  and (c)  $\tan(\varphi)$  of the Fo7 measured under water saturation three effective pressures of  $P_{\text{eff}} = [1; 2.5; 5]$  MPa. The  $\nu$  values of the dry sample are reported for comparison for the three pressures.

$$\begin{cases} \epsilon_{\text{ax}}^* = \frac{1}{E} \sigma_{\text{ax}} + \frac{\alpha}{3K} p_f, \\ \epsilon_{\text{rad}}^* = -\frac{\nu}{E} \sigma_{\text{ax}} + \frac{\alpha}{3K} p_f, \end{cases} \quad (10)$$

with  $E$  and  $K$  being the drained rock's elastic moduli,  $\nu$  the drained Poisson's ratio, and  $\alpha$  the Biot coefficient.

The Biot coefficient  $\alpha$  can be calculated in the framework of the poroelastic theory from the drained (i.e.,  $K \sim 10$  GPa) and skeleton (i.e.,  $K_s \sim 37$  GPa) bulk moduli such that  $\alpha = 1 - K/K_s$  (i.e.,  $\alpha \sim 0.73$ ). As  $p_f$  oscillations are of  $10^{-2}$  MPa for  $\sigma_{\text{ax}}$  oscillations of  $10^{-1}$  MPa (see Figure 10 from Pimienta et al., 2015b),  $p_f$  contribution to the axial deformation is  $(\alpha/3K)p_f \sim 10^{-6}$ , that is, 10 times smaller than  $\sigma_{\text{ax}}/E$ . But, because  $\nu$  is close to 0.1,  $p_f$  contribution to the radial deformation is comparable to  $\nu\sigma_{\text{ax}}/E$ . Thus, in practice we record an “apparent Poisson's ratio”  $\nu_{\text{app}}$  defined as follows:

$$\nu_{\text{app}} = -\frac{\frac{-\nu}{E}\sigma_{\text{ax}} + \frac{\alpha}{3K}p_f}{\frac{1}{E}\sigma_{\text{ax}} + \frac{\alpha}{3K}p_f}. \quad (11)$$

As a first-order approximation, we assume the local pore pressure  $p_f$  by the gauge to be equal to the one measured experimentally at the sample's outlet. The correction is directly applied to the strain measurement (equation 10), leading to new values of Young's modulus and Poisson's ratio (Figure 6a) and the phase shifts (i.e.,  $Q_E^{-1}$  and  $\tan(\phi)$ ). As shown from the example, Young's modulus is only slightly affected by this poroelastic correction, and it decreases by approximately 5% (Figure 6a). However, the sample Poisson's ratio is more affected and decreases by up to 30% after the correction (Figure 6a). The slope of the linear regression changes, and a strong hysteresis is observed on this corrected value, indicating a higher  $\tan(\phi)$  peak.

The frequency dependence of the directly measured and corrected  $\nu$  (Figure 6b) and  $\tan(\phi)$  (Figure 6c) are compared for effective pressures below 10 MPa. For all effective pressures, the corrected values at lower frequencies are lower than the uncorrected ones. The corrected “drained” value is close to the “dry” one, as predicted by poroelasticity. Because  $K_d$  increases (and  $\alpha$  decreases) with increasing  $P_{\text{eff}}$ , the difference between measured and corrected values decreases at higher pressures. A stronger  $\tan(\phi)$  peak, as high as approximately 0.5 at  $P_{\text{eff}} = 1$  MPa, is inferred in the case of the drained/undrained transition (Figure 6c).

### Effective medium theories: Values of $\nu$ in the three elastic regimes

Starting from Biot (1956a, 1956b), several models have been developed to account for the fluid effect on the different elastic regimes in isotropic (e.g., Mavko and Jizba, 1991, 1994; Le Ravalec et al., 1996; Le Ravalec and Guéguen, 1996) or anisotropic (e.g., Guéguen and Kachanov, 2011; Collet and Gurevich, 2013) rocks. The critical frequency of these different regimes has been discussed (O'Connell and Budiansky, 1974; Mavko and Nur, 1975; Cleary, 1978). Models have been developed for the transition between those regimes (Müller et al., 2010). Our purpose is to check the consistency of the measurements, with EMTs. The approach of Adelin et al. (2011) can be used to calculate the  $\nu$  values for the three elastic regimes (i.e., drained, undrained, and unrelaxed regimes) that are expected in the investigated frequency range of  $f \in [10^{-3}, 10^6]$  Hz.

The approach of Adelin et al. (2011) combines the Biot-Gassmann and EMTs. Adelin et al. (2010, 2011) have investigated basalts composed of a large amount of equant pores and a small quantity of microcracks. Sedimentary rocks also exhibit a microstructure that can schematically be considered as made of equant pores and compliant microcracks (e.g., Fortin et al., 2007; Guéguen and Kachanov, 2011; Pimienta et al., 2014). Using the model of Le Ravalec and Guéguen (1996), the drained (i.e.,  $K_d$  and  $G_d$ ) and unrelaxed (i.e.,  $K_{\text{ur}}$  and  $G_{\text{ur}}$ ) regimes are built by predicting, respectively, the effective elastic properties of the dry and fluid-saturated medium. The intermediate undrained regime (i.e.,  $K_{\text{ud}}$  and  $G_{\text{ud}} = G_d$ ) is then attained from the drained one using Biot-Gassmann fluid substitution theory, accounting for the contribution of pores  $\phi_p$  and cracks  $\phi_c$ . Poisson's ratio  $\nu$  is estimated from  $K$  and  $G$  using the relations of linear elasticity in isotropic media (Mavko et al., 2003).

For a clastic rock, the dominant microstructural parameters affecting elasticity are the microcrack density  $\rho$  and aspect ratio  $\xi$  (e.g., Guéguen and Kachanov, 2011). The main parameter is  $\rho$ , and its variations account for the pressure dependence of elastic properties (Walsh, 1965). To better compare measurements and calculations, one needs first to investigate the relationship between the microstructural parameters and effective pressure.

#### Microcrack density and aspect ratio

Microstructural parameters  $\rho$  and  $\xi$  may be inverted from the measured dry and water-saturated P-wave velocities (e.g., Fortin

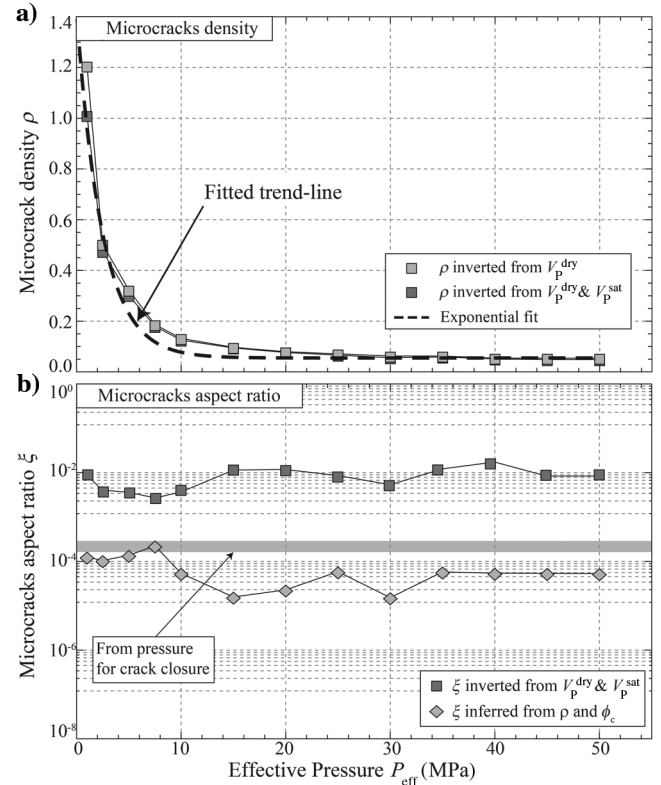


Figure 7. Inverted microcrack (a) density  $\rho$  and (b) aspect ratio  $\xi$  as a function of effective confining pressure. The  $\rho$  is inverted using measurements under either dry or dry and water-saturated conditions. The  $\xi$  is either inverted from the measurements under dry and water-saturated conditions or inferred from the inverted  $\rho$  and the measured porosity variation.

et al., 2007; Pimienta et al., 2014). For this inversion, the Fo7 sample's porosity (7%) is chosen, and  $K_S$  and  $G_S$  are those of quartz (Mavko et al., 2003). This straightforward modeling approach involves assuming the noninteraction approximation, an assumption known to be inexact in the case of large microcrack densities. The inversion of the P-wave velocities in terms of microcrack density and aspect ratio is shown in Figure 7.

A large decrease in  $\rho$  is observed as  $P_{\text{eff}}$  increases (Figure 7a), which originates from the progressive closure of microcracks with increasing  $P_{\text{eff}}$  (Walsh, 1965). Because the rock sample bears a large amount of microcracks and is measured down to very low effective pressures, the model's limits are reached so that  $\rho$  is overestimated at  $P_{\text{eff}}$  lower than 2.5–5 MPa.

Parameter  $\xi$  remains constant for all  $P_{\text{eff}}$  (Figure 7b), which results from the low sensitivity to  $\xi$  as long as  $\xi < 10^{-2}$ . The  $\xi$  can also be inferred using two other methods, that is, using the crack closing pressure theory (Walsh, 1965) or the measured pressure-dependent porosity variations that correspond to the crack porosity  $\phi_c$ . These methods give the same result in the range of  $\xi \sim 1\text{--}5 \cdot 10^{-4}$ , a value lower than that inferred from using the EMT. The real value for the mean  $\xi$  is probably of  $\xi \sim 10^{-3}$  or slightly lower.

### Poisson's ratio for the three elastic regimes

Microcrack density values (Figure 7a) are used to directly calculate the variations of Poisson's ratio for the three regimes as a function of  $P_{\text{eff}}$  (Figure 8). For this prediction,  $K_S$  and  $G_S$  are the ones of the quartz (Mavko et al., 2003), and  $\nu_{\text{ud}}$  and  $\nu_{\text{ur}}$  are predicted for water- and glycerin-saturated media. Although the drained  $\nu_d$  depends only on  $\rho$ ,  $\nu_{\text{ud}}$  and  $\nu_{\text{ur}}$  depend on  $\rho$  and  $\xi$ ;  $\nu_{\text{ud}}$  is calculated for a value of  $\xi = 10^{-3}$ , and  $\nu_{\text{ur}}$  is calculated for values of  $10^{-3}$  and  $10^{-2}$ .

Poisson's ratio is calculated for either (1) a purely microcracked medium (Figure 8a), that is, with no equant pore, or (2) a porous and microcracked medium (Figure 8b), that is, with cracks and equant pores. For both cases, as a result of the cracks' closure,  $\nu_d$  increases with  $P_{\text{eff}}$  and a large decrease is observed for  $\nu_{\text{ud}}$  and  $\nu_{\text{ur}}$  as  $P_{\text{eff}}$  increases. Note that porosity affects mainly the calculated  $\nu_{\text{ud}}$ , as expected from the Biot-Gassmann equation. Interestingly, for both media, the calculated undrained  $\nu_{\text{ud}}$  is larger than the unrelaxed  $\nu_{\text{ur}}$  at low  $P_{\text{eff}}$ . Then, the relation  $\nu_d < \nu_{\text{ur}} < \nu_{\text{ud}}$  is found. The same relation between the three regimes has been previously reported for a purely microcracked medium (see Figure 2 of Wang et al., 2012). Note that a strong dependence on the saturating fluid bulk modulus is predicted only if equant pores are present (Figure 8b). The effect is particularly

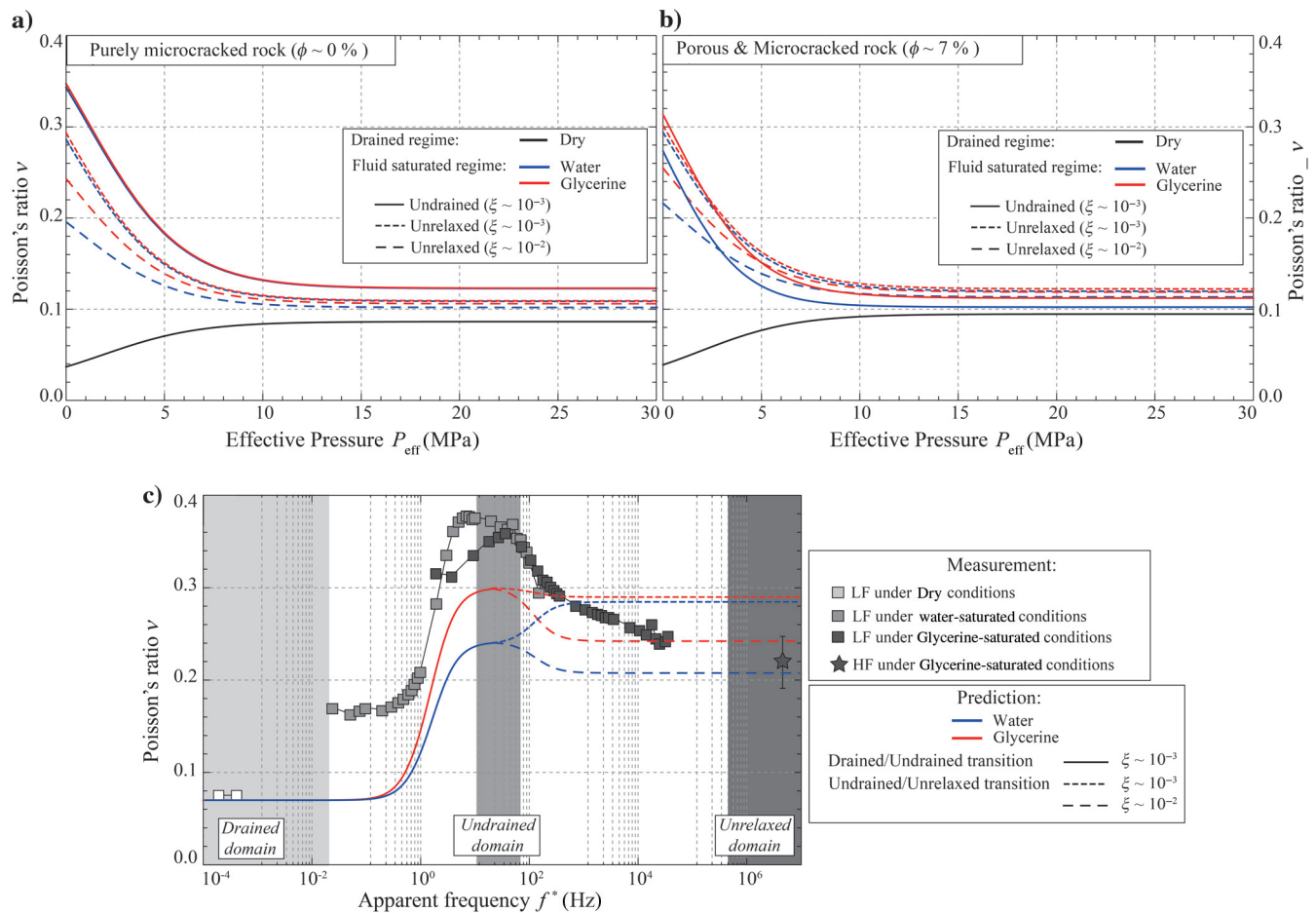


Figure 8. Calculated Poisson's ratio for the drained, undrained, and unrelaxed regimes. Two scenarios are tested: (a) a microcracked rock and (b) a porous and microcracked rock. (c) Comparison between measured (symbols) and calculated Poisson's ratio as a function of  $f^*$  for the Fo7 sample at  $P_{\text{eff}} = 1$  MPa. A Zener model is used to obtain the transition between the predicted regimes.

strong for the  $\nu_{ud}$  prediction. This, again, is expected from the Gassmann equation. When equant pores and cracks are present, the range of pressure in which the inequality  $\nu_{ur} < \nu_{ud}$  depends on the exact  $\xi$  values.

Because the unrelaxed regime is expected to take place at higher frequencies than the undrained one, the relation  $\nu_d < \nu_{ur} < \nu_{ud}$  explains the measured bell-shaped variations for  $\nu$ . To account for the frequency dependence, a simple Zener model is used (e.g., Pimienta

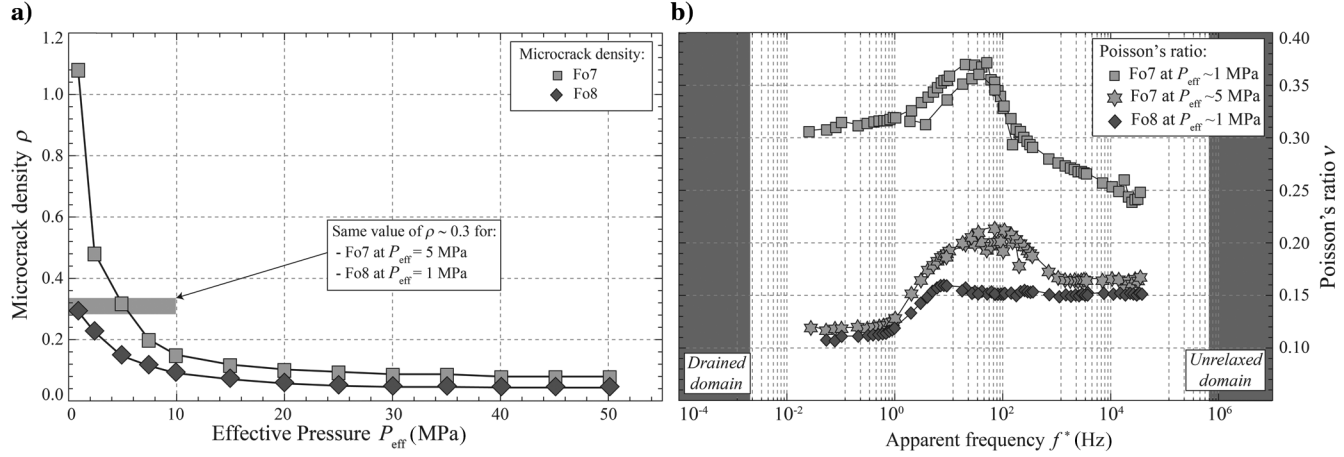


Figure 9. Comparison between Fo7 and Fo8 samples: (a) inverted microcrack density as a function of effective pressure and (b) dependence of Poisson's ratio to  $f^*$  for the Fo7 and Fo8 samples. In panel (b), only the measurement at  $P_{\text{eff}} = 1$  MPa is reported for the Fo8 sample, and measurements at  $P_{\text{eff}} = 1$  MPa (i.e., squares) and  $P_{\text{eff}} = 5$  MPa (i.e., stars) are reported for Fo7 sample.

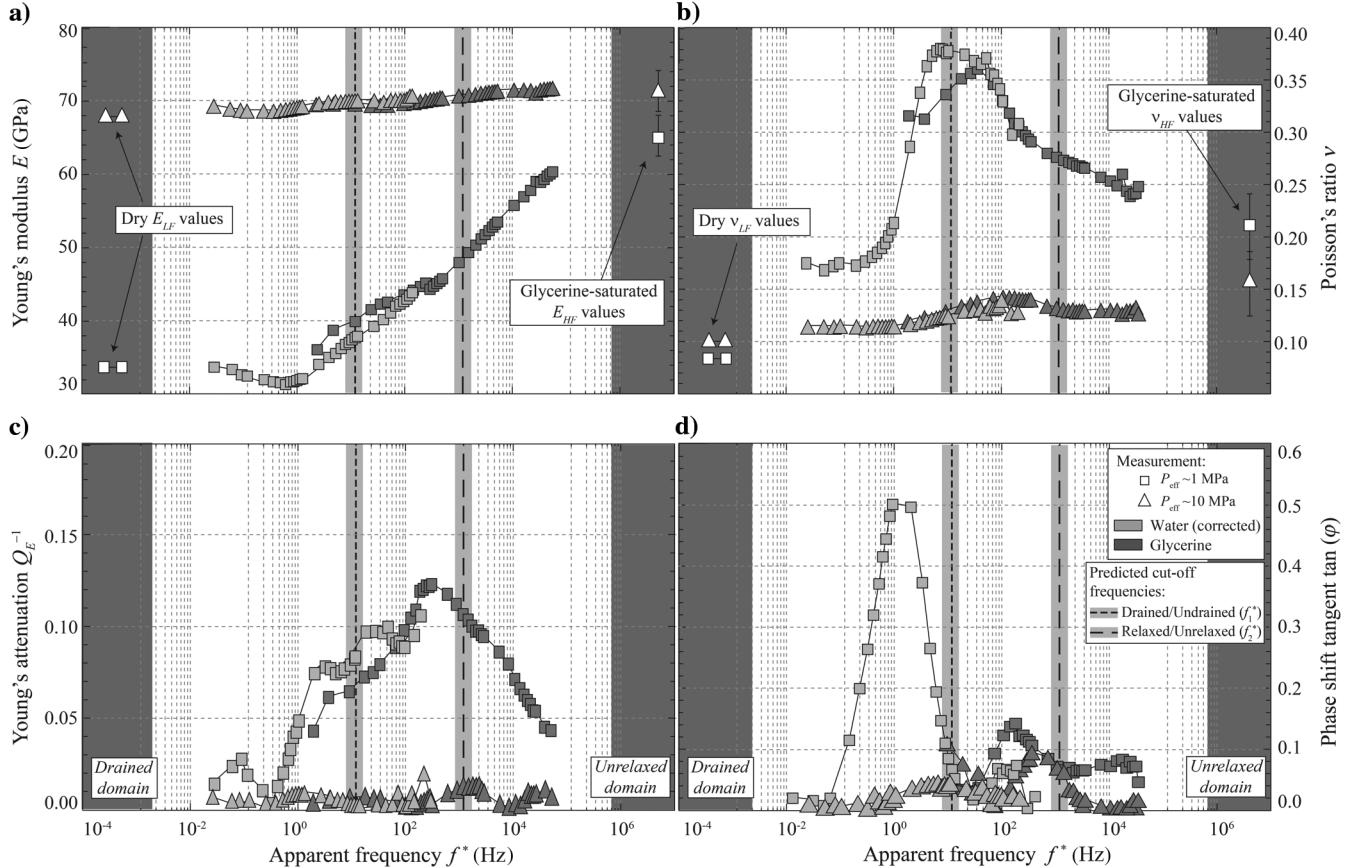


Figure 10. Comparison for sample Fo7 of the dependence to  $f^*$  of (a) Young's modulus  $E$ , (b) Poisson's ratio  $\nu$ , and their related dissipations, that is, (c)  $Q_E^{-1}$  and (d)  $\tan(\phi)$ . The measurements are reported for two effective pressures of 1 and 10 MPa. The predicted cutoff frequencies  $f_1^* = 10$  Hz and  $f_2^* = 1$  kHz are reported for comparison. Note that the scale is not the same for the dissipations on (c)  $E$  and (d)  $\nu$ .

et al., 2015a). The model compares favorably with the data (Figure 8c). For both undrained and unrelaxed regimes, the predicted magnitude of variation is consistent with the measurements.

The above model provides a reasonable explanation of the existence of a bell-shaped variation for  $\nu$ . However, the agreement between measurements and calculations (Figure 8c) is not perfect:  $\nu_{ud}$  in particular is underestimated by the model. The discrepancies might result from the experimental conditions (e.g., the use of jacked samples and the existence of a dead volume) and the approximations of the model.

## DISCUSSION

In the following, we examine further the contrasted behavior of Fo7 and Fo8 samples. We also discuss the results of Pimienta et al. (2015b), by comparing them to the present data on Poisson's ratio. We finally shortly discuss our results in terms of  $V_p/V_s$  ratio.

### Case of the Fo8 sample

As shown from Figure 2, although Fo7 and Fo8 samples have a very similar porosity, their saturated Poisson's ratio is very different. To test the role of microcrack density in both Fo7 and Fo8 samples, effective medium theories are used to invert the microcrack density (Figure 9a). The dependence to  $f^*$  of both rocks' Poisson's ratio is compared (Figure 9b).

For the Fo8 sample, the maximum value of the crack density is 0.3 at  $P_{eff} = 1$  MPa (Figure 9a), that is, much lower than the Fo7 sample. Note that  $\nu$  of Fo8 at  $P_{eff} = 1$  MPa shows a small increase with  $f^*$  up to a value of approximately  $\nu \sim 0.15$ . At the highest frequency, this value of  $\nu$  is very similar to the one of Fo7 at  $P_{eff} = 5$  MPa. Interestingly, the crack density inverted at these pressures (i.e.,  $P_{eff} = 1$  MPa for Fo8 and  $P_{eff} = 5$  MPa for Fo7) is of approximately  $\rho = 0.3$  for both rocks. Thus, the values of  $\nu_{ur}$  strongly relate to the sample's microcrack density.

Note further that  $\nu$  of Fo8 remains constant at frequencies beyond 5 Hz. This observation is consistent with the result of Pimienta et al. (2015a). In the case of the Fo8 sample, the two cutoff frequencies  $f_1^*$  and  $f_2^*$  overlap. For the Fo8 sample, there is a direct transition from the drained to the unrelaxed regime.

### Comparison with Young's modulus

#### Dispersion and attenuation

Young's modulus and Poisson's ratio are two independent elastic parameters. It is, however, possible to compare their frequency-dependent behavior. The Young's modulus frequency dependence has been measured for Fo7 and Fo8 samples for different saturating fluids and at different effective pressures in a previous paper (Pimienta et al., 2015b).

As indicated above, the Fo8 sample does not show important frequency-dependent variations of Young's modulus and Poisson's ratio. Thus, we investigate the Fo7 sample only. Young's modulus (Figure 10a), Poisson's ratio (Figure 10b), and their related dissipations (Figure 10c and 10d) measured on Fo7 saturated by different fluids are reported as a function of  $f^*$  for two effective pressures of 1 and 10 MPa. For consistency with reported Poisson's ratio data, the poroelastic correction discussed above (Figure 6a) is also applied to Young's modulus data.

Confining pressure strongly damps the measured dispersions/attenuations, so that almost no frequency dependence is observed beyond  $P_{eff} = 10$  MPa. This is due to the crack closure. But strong dispersion/attenuation phenomena are observed at  $P_{eff} = 1$  MPa. The measured  $E$  dispersion is in agreement with the calculated critical frequencies  $f_1^* = 10$  Hz and  $f_2^* = 1$  kHz. It has been shown earlier that Poisson's ratio dispersion and dissipation exhibit two transitions at frequencies of approximately 5 and 500 Hz. These frequencies are lower than the above ones, but the discrepancies are small.

Note finally that the magnitude of dissipation for  $\nu$  (Figure 10d) is larger than for  $E$  (Figure 10c) at frequencies lower than 100 Hz, that is, for the drained/undrained transition. For the undrained/unrelaxed transition (i.e., above 100 Hz) these dissipations show similar magnitudes. Indeed, large dispersions/attenuations have been observed for  $K$  for the drained/undrained transition (Pimienta et al., 2015a). Given that no dissipation is expected for  $G$  (i.e.,  $G^* = G$ ) for this transition (e.g., Gassmann, 1951), and given that  $E^* = 2 G^*(1 + \nu^*)$ , equation 6 simplifies to  $Q_E^{-1} \sim x Q_\nu^{-1}$ . Because  $x = (E_1/G_1) - 1$  is similar to a rock Poisson's ratio, and thus in the range of  $0 < x < 0.5$ , it can be concluded that  $Q_\nu^{-1} \gg Q_E^{-1}$ . This is in agreement with our measurements.

#### Comparison with effective medium theories

Using EMTs and the same parameters as in Figure 8c, the variations of Young's modulus of Fo7 sample at  $P_{eff} = 1$  MPa are calculated. Then, the calculated dispersions are compared with the measured ones (Figure 11).

The calculated  $E$  underestimates the measured one for undrained and unrelaxed regimes. This discrepancy may be due to an underestimated elastic dispersion in  $G$  in the unrelaxed.

### Frequency dependence of the $V_p/V_s$ ratio

When comparing field to lab measurements, the  $V_p/V_s$  ratio is the rock property that needs to be investigated. Noting that a direct relationship links  $V_p/V_s$  to the rock Poisson's ratio  $\nu$  in an elastic isotropic homogeneous medium (e.g., Wang et al., 2012), the in-

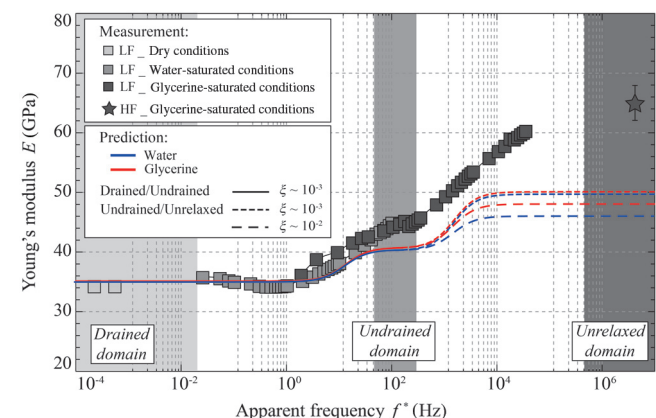


Figure 11. Comparison between measured (Pimienta et al., 2015b) and calculated Young's modulus for the Fo7 sample at  $P_{eff} = 1$  MPa. The exact same model parameters as in Figure 8c are used here. The three distinct drained, undrained, and unrelaxed regimes are highlighted in gray zones.

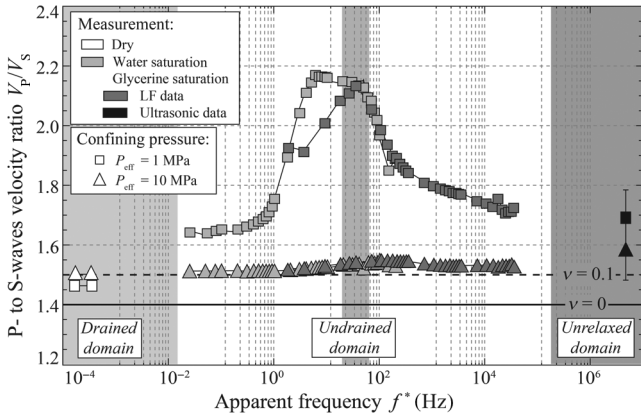


Figure 12.  $V_p/V_s$  ratio, inferred from the corrected Poisson's ratio, as a function of  $f^*$  for the fluid-saturated Fo7 sample at confining pressures of  $P_{\text{eff}} = 1 \text{ MPa}$  and  $P_{\text{eff}} = 10 \text{ MPa}$ . Values for  $\nu = 0$  (thick line) and  $\nu = 0.1$  (dashed line) are reported for reference.

ferred  $V_p/V_s$  ratio can be calculated in the seismic frequency range (Figure 12).

Interestingly, the same bell-shaped variations are calculated for the  $V_p/V_s$  ratio as  $f^*$  increases, with a maximum value of 2.2 for the undrained regime. The magnitudes of the variations largely decrease with increasing effective pressure, and they are constant at 1.5 (i.e.,  $\nu = 0.1$ ) beyond  $P_{\text{eff}} = 10 \text{ MPa}$ .

## CONCLUSION

The stress-strain method has been applied to measure the frequency-dependent Poisson's ratio dispersion in sandstones. Testing the method on standard samples shows that the experimental setup gives reliable results. The measured frequency-dependent variations in  $\nu$  correlate with peaks in the phase shift  $\tan(\varphi)$ . Pressure- and frequency-dependent  $\nu$  has been investigated on sandstones under dry and fluid-saturated conditions. Large dependences to fluids, pressures and frequencies are observed, and frequency-dependent bell-shaped variations have been measured for one sample. The fluid viscosity plays a major role on the frequency dependence of the variations, and the rock crack density plays a major role on the magnitude of the variations.

Accounting for the fluid viscosity, an apparent frequency  $f^*$  is defined, and its frequency range is  $f^* \in [10^{-3}; 10^5] \text{ Hz}$ . The measured variations are shown to be consistent with a theoretical interpretation using the fluid flow, effective medium, and poroelastic theories. For the sample showing the bell-shaped variations, two dispersion phenomena are clearly evidenced. The cutoff frequencies match fluid-flow theories predictions for both drained/undrained and undrained/unrelaxed transitions. The bell-shaped, frequency-dependent variation of  $\nu$  in this sample is explained using EMTs. This implies that, depending on their microcrack density, some rocks may have an undrained Poisson's ratio (i.e.,  $\nu_{\text{ud}}$ ) larger than the unrelaxed one (i.e.,  $\nu_{\text{ur}}$ ) such that  $\nu_d < \nu_{\text{ur}} < \nu_{\text{ud}}$ . It implies that Poisson's ratio seems to be a good proxy of the transitions between elastic regimes.

## ACKNOWLEDGMENTS

This work has been partially supported by Total, under project no. FR00007429. The authors thank Y. Pinquier and A. Schubnel

for their technical help in setting up the system. The authors also thank L. Adam, B. Gurevitch, and two anonymous reviewers for their constructive comments. Finally, the first author wishes to thank F. X. Passelegue for the scientific discussions.

## REFERENCES

- Adam, L., and M. Batzle, 2008, Elastic properties of carbonates from laboratory measurements at seismic and ultrasonic frequencies: The Leading Edge, **27**, 1026–1032.
- Adam, L., M. Batzle, and I. Brevik, 2006, Gassmann's fluid substitution and shear modulus variability in carbonates at laboratory seismic and ultrasonic frequencies: Geophysics, **71**, no. 6, F173–F183, doi: [10.1190/1.2358494](https://doi.org/10.1190/1.2358494).
- Adam, L., M. Batzle, K. Lewallen, and K. van Wijk, 2009, Seismic wave attenuation in carbonates: Journal of Geophysical Research, **114**, B06208.
- Adelinet, M., J. Fortin, and Y. Guéguen, 2011, Dispersion of elastic moduli in a porous-cracked rock: Theoretical predictions for squirt-flow: Tectonophysics, **503**, 173–181, doi: [10.1016/j.tecto.2010.10.012](https://doi.org/10.1016/j.tecto.2010.10.012).
- Adelinet, M., J. Fortin, Y. Guéguen, A. Schubnel, and L. Geoffroy, 2010, Frequency and fluid effects on elastic properties of basalt: Experimental investigations: Geophysical Research Letters, **37**, L02303, doi: [10.1029/2009GL041660](https://doi.org/10.1029/2009GL041660).
- Batzle, M. L., D.-H. Han, and R. Hofmann, 2006, Fluid mobility and frequency-dependent seismic velocity — Direct measurements: Geophysics, **71**, no. 1, N1–N9, doi: [10.1190/1.2159053](https://doi.org/10.1190/1.2159053).
- Batzle, M., R. Hofmann, D.-H. Han, and J. Castagna, 2001, Fluids and frequency dependent seismic velocity of rocks: The Leading Edge, **20**, 168–171, doi: [10.1190/1.1438900](https://doi.org/10.1190/1.1438900).
- Biot, M. A., 1956a, Theory of propagation of elastic waves in a fluid-saturated porous solid — I: Low-frequency range: The Journal of the Acoustical Society of America, **28**, 168–178, doi: [10.1121/1.1908239](https://doi.org/10.1121/1.1908239).
- Biot, M. A., 1956b, Theory of propagation of elastic waves in a fluid-saturated porous solid — II: Higher frequency range: The Journal of the Acoustical Society of America, **28**, 179–191, doi: [10.1121/1.1908241](https://doi.org/10.1121/1.1908241).
- Boudet, J., and S. Ciliberto, 1998, Interaction of sound with fast crack propagation: Physical Review Letters, **80**, 341–344, doi: [10.1103/PhysRevLett.80.341](https://doi.org/10.1103/PhysRevLett.80.341).
- Bourbie, T., and B. Zinszner, 1985, Hydraulic and acoustic properties as a function of porosity in Fontainebleau sandstone: Journal of Geophysical Research: Solid Earth (1978–2012), **90**, 11524–11532.
- Brantut, N., A. Schubnel, E. David, E. Héripé, Y. Guéguen, and A. Dimanov, 2012, Dehydration-induced damage and deformation in gypsum and implications for subduction zone processes: Journal of Geophysical Research: Solid Earth (1978–2012), **117**, B3, doi: [10.1029/2011JB008730](https://doi.org/10.1029/2011JB008730).
- Cleary, M. P., 1978, Elastic and dynamic response regimes of fluid-impregnated solids with diverse microstructures: International Journal of Solids and Structures, **14**, 795–819, doi: [10.1016/0020-7683\(78\)90072-0](https://doi.org/10.1016/0020-7683(78)90072-0).
- Collet, O., and B. Gurevich, 2013, Fluid dependence of anisotropy parameters in weakly anisotropic porous media: Geophysics, **78**, no. 5, WC137–WC145, doi: [10.1190/geo2012-0499.1](https://doi.org/10.1190/geo2012-0499.1).
- David, E. C., J. Fortin, A. Schubnel, Y. Guéguen, and R.W. Zimmerman, 2013, Laboratory measurements of low-and high-frequency elastic moduli in Fontainebleau sandstone: Geophysics, **78**, no. 5, D369–D379, doi: [10.1190/geo2013-0070.1](https://doi.org/10.1190/geo2013-0070.1).
- Detournay, E., and A. H-D. Cheng, 1993, Fundamentals of poroelasticity, vol. 2: Analysis and design method: Pergamon Press.
- Dunn, K.-J., 1987, Sample boundary effect in acoustic attenuation of fluid-saturated porous cylinders: The Journal of the Acoustical Society of America, **81**, 1259, doi: [10.1121/1.394529](https://doi.org/10.1121/1.394529).
- Fortin, J., Y. Guéguen, and A. Schubnel, 2007, Effects of pore collapse and grain crushing on ultrasonic velocities and  $V_p/V_s$ : Journal of Geophysical Research: Solid Earth (1978–2012), **112**, B8, doi: [10.1029/2005JB004005](https://doi.org/10.1029/2005JB004005).
- Fortin, J., L. Pimienta, Y. Guéguen, A. Schubnel, E. David, and M. Adelinet, 2014, Experimental results on the combined effects of frequency and pressure on the dispersion of elastic waves in porous rocks: The Leading Edge, **33**, 648–654, doi: [10.1190/tle33060648.1](https://doi.org/10.1190/tle33060648.1).
- Gassmann, F., 1951, Elasticity of porous media: Vierteljahrsschrder Naturforschenden Gesellschaft, **96**, 1–23.
- Gomez, C., J. Dvorkin, and T. Vanorio, 2010, Laboratory measurements of porosity, permeability, resistivity, and velocity on Fontainebleau sandstones: Geophysics, **75**, no. 6, E191–E204, doi: [10.1190/1.3493633](https://doi.org/10.1190/1.3493633).
- Guéguen, Y., and M. Kachanov, 2011, Effective elastic properties of cracked rocks — An overview, in Y. M. Leroy, and F. K. Lehner, eds., Mechanics of crustal rocks: Springer, 73–125.
- Jackson, I., and M. Paterson, 1987, Shear modulus and internal friction of calcite rocks at seismic frequencies: Pressure, frequency and grain size

- dependence: Physics of the Earth and Planetary Interiors, **45**, 349–367, doi: [10.1016/0031-9201\(87\)90042-2](https://doi.org/10.1016/0031-9201(87)90042-2).
- Le Ravalec, M., and Y. Guéguen, 1996, High-and low-frequency elastic moduli for a saturated porous/cracked rock-differential self-consistent and poroelastic theories: Geophysics, **61**, 1080–1094, doi: [10.1190/1.1444029](https://doi.org/10.1190/1.1444029).
- Le Ravalec, M., Y. Guéguen, and T. Chelidze, 1996, Elastic wave velocities in partially saturated rocks: Saturation hysteresis: Journal of Geophysical Research, **101**, 837–844, doi: [10.1029/95JB02879](https://doi.org/10.1029/95JB02879).
- Madonna, C., and N. Tisato, 2013, A new seismic wave attenuation module to experimentally measure low-frequency attenuation in extensional mode: Geophysical Prospecting, **61**, 302–314, doi: [10.1111/gpr.2013.61.issue-2](https://doi.org/10.1111/gpr.2013.61.issue-2).
- Madonna, C., N. Tisato, B. Artman, and E. Saenger, 2011, Laboratory measurements of seismic attenuation from 0.01 to 100 Hz: 73rd Annual International Conference and Exhibition, EAGE, Extended Abstracts, doi: [10.3997/2214-4609.20149425](https://doi.org/10.3997/2214-4609.20149425).
- Mallet, C., J. Fortin, Y. Guéguen, and F. Bouyer, 2013, Effective elastic properties of cracked solids: An experimental investigation: International journal of fracture, **182**, 275–282, doi: [10.1007/s10704-013-9855-y](https://doi.org/10.1007/s10704-013-9855-y).
- Mavko, G., and D. Jizba, 1991, Estimating grain-scale fluid effects on velocity dispersion in rocks: Geophysics, **56**, 1940–1949, doi: [10.1190/1.1443005](https://doi.org/10.1190/1.1443005).
- Mavko, G., and D. Jizba, 1994, The relation between seismic P-and S-wave velocity dispersion in saturated rocks: Geophysics, **59**, 87–92, doi: [10.1190/1.1443537](https://doi.org/10.1190/1.1443537).
- Mavko, G., T. Mukerji, and J. Dvorkin, 2003, The rock physics handbook: Tools for seismic analysis of porous media: Cambridge University Press.
- Mavko, G., and A. Nur, 1975, Melt squirt in the asthenosphere: Journal of Geophysical Research, **80**, 1444–1448, doi: [10.1029/JB080i011p01444](https://doi.org/10.1029/JB080i011p01444).
- Mikhailsevitch, V., M. Lebedev, and B. Gurevich, 2014, A laboratory study of low-frequency wave dispersion and attenuation in water-saturated sandstones: The Leading Edge, **33**, 616–622, doi: [10.1190/tle33060616.1](https://doi.org/10.1190/tle33060616.1).
- Mikhailsevitch, V., M. Lebedev, and B. Gurevich, 2011, A low-frequency laboratory apparatus for measuring elastic and anelastic properties of rocks: 81st Annual International Meeting, SEG, Expanded Abstracts, 2256–2260.
- Mikhailsevitch, V., M. Lebedev, and B. Gurevich, 2013, Laboratory measurements of the elastic and anelastic parameters of limestone at seismic frequencies: 83rd Annual International Meeting, SEG, Expanded Abstracts, 2974–2978.
- Müller, T. M., B. Gurevich, and M. Lebedev, 2010, Seismic wave attenuation and dispersion resulting from wave-induced flow in porous rocks — A review: Geophysics, **75**, no. 5, 75A147–75A164, doi: [10.1190/1.3463417](https://doi.org/10.1190/1.3463417).
- O'Connell, R. J., and B. Budiansky, 1974, Seismic velocities in dry and saturated cracked solids: Journal of Geophysical Research, **79**, 5412–5426, doi: [10.1029/JB079i035p05412](https://doi.org/10.1029/JB079i035p05412).
- O'Connell, R. J., and B. Budiansky, 1977, Viscoelastic properties of fluid-saturated cracked solids: Journal of Geophysical Research, **82**, 5719–5735, doi: [10.1029/JB082i036p05719](https://doi.org/10.1029/JB082i036p05719).
- Pimienta, L., J. Fortin, and Y. Guéguen, 2015a, Bulk modulus dispersion and attenuation in sandstones: Geophysics, **80**, no. 2, D111–D127, doi: [10.1190/geo2014-0335.1](https://doi.org/10.1190/geo2014-0335.1).
- Pimienta, L., J. Fortin, and Y. Guéguen, 2015b, Young modulus dispersion and attenuation in sandstones: Geophysics, **80**, no. 5, L57–L72, doi: [10.1190/geo2014-0532.1](https://doi.org/10.1190/geo2014-0532.1).
- Pimienta, L., J. Sarout, L. Esteban, and C. Delle Piane, 2014, Prediction of rocks thermal conductivity from elastic wave velocities, mineralogy and microstructure: Geophysical Journal International, **197**, 860–874, doi: [10.1093/gji/ggu034](https://doi.org/10.1093/gji/ggu034).
- Sarout, J., 2012, Impact of pore space topology on permeability, cut-off frequencies and validity of wave propagation theories: Geophysical Journal International, **189**, 481–492, doi: [10.1111/gji.2012.189.issue-1](https://doi.org/10.1111/gji.2012.189.issue-1).
- Subramanyan, S., B. Quintal, N. Tisato, E.H. Saenger, and C. Madonna, 2014, An overview of laboratory apparatuses to measure seismic attenuation in reservoir rocks: Geophysical Prospecting, **62**, 1211–1223, doi: [10.1111/gpr.2014.62.issue-6](https://doi.org/10.1111/gpr.2014.62.issue-6).
- Tisato, N., and C. Madonna, 2012, Attenuation at low seismic frequencies in partially saturated rocks: Measurements and description of a new apparatus: Journal of Applied Geophysics, **86**, 44–53, doi: [10.1016/j.jappgeo.2012.07.008](https://doi.org/10.1016/j.jappgeo.2012.07.008).
- Walsh, J. B., 1965, The effect of cracks on the compressibility of rocks: Journal of Geophysical Research, **71**, 2591–2599, doi: [10.1029/JZ071i010p02591](https://doi.org/10.1029/JZ071i010p02591).
- Wang, X.-Q., A. Schubnel, J. Fortin, E. David, Y. Guéguen, and H.-K. Ge, 2012, High  $V_P/V_S$  ratio: Saturated cracks or anisotropy effects? Geophysical Research Letters, **39**, 11, doi: [10.1029/2012GL051742](https://doi.org/10.1029/2012GL051742).
- Winkler, K., 1983, Contact stiffness in granular porous materials: Comparison between theory and experiment: Geophysical Research Letters, **10**, 1073–1076, doi: [10.1029/GL010i011p01073](https://doi.org/10.1029/GL010i011p01073).
- Winkler, K. W., and W. F. Murphy, 1995, Acoustic velocity and attenuation in porous rocks: Rock physics and phase relations: Reference Shelf 3: AGU.
- Winkler, K., and A. Nur, 1979, Pore fluids and seismic attenuation in rocks: Geophysical Research Letters, **6**, 1–4, doi: [10.1029/GL006i001p00001](https://doi.org/10.1029/GL006i001p00001).